Direct double photoionization of the valence shell of Be

F. Citrini, L. Malegat, and P. Selles
Laboratoire d'Interaction du Rayonnement X avec la Matière (UMR 8624 du CNRS), Université Paris–Sud, Batiment 350, 91405 Orsay Cedex, France

A. K. Kazansky
Fock Institute of Physics, The University of St. Petersburg, St. Petersburg 198504, Russia
(Received 16 December 2002; published 17 April 2003)

The hyperspherical $\mathcal{R}$-matrix method with semiclassical outgoing waves is used to study the direct double photoionization (DPI) of the valence shell of the lightest alkaline earth-metal Be. The absolute fully integrated, singly, doubly, and triply differential cross sections obtained are compared with the single set of measurements available and with recent calculations based on the convergent close coupling and time-dependent close coupling methods. The level of agreement between all these data is very encouraging. A comparison is also made between the DPI of He and the direct DPI of the valence shell of Be. It confirms that the electron-electron correlations are stronger in the valence $2s$ shell of Be than in the $1s$ shell of He, thus contributing to a desirable clarification.

DOI: 10.1103/PhysRevA.67.042709 PACS number(s): 32.80.Fb

I. INTRODUCTION

The DPI (double photoionization) of He is one of the most suitable processes to study electronic correlations in the continuum. Accordingly, it has been the subject of intensive research over the past decades, both theoretically and experimentally. Absolute measurements of the associated fully differential cross sections, referred to as TDCSs (triply differential cross sections), are now available [1–3]. The first ones [1] are reproduced satisfactorily by the most recent *ab initio* theories, namely the CCC (convergent close coupling) [1], the TDCC (time-dependent close coupling) [4], and the HRM-SOW (hyperspherical R-matrix method with semiclassical outgoing waves) [5]. However, in many cases where only relative measurements are available, these various methods provide absolute scales that still differ from each other significantly. In addition, challenging dynamical situations have been characterized, where most theories fail to reproduce even the shapes of the measured TDCSs [6]. Despite these lasting difficulties on He, which require still more efforts of experimentalists and theorists, the interest has begun to move to alternative targets.

Alkaline-earth-metal atoms, with a diffuse and weakly bound ns^2 valence shell outside a compact and tightly bound closed-shell core, represent the next level of complexity from the theoretical point of view: actually, the direct DPI of the valence shell is likely to be described reasonably well within a two-electron approach, based on a modelization of the core-valence interaction.

Preliminary calculations were performed as early as 1994 [7], but only in 1997 qualitatively reasonable results were obtained within the extended Wannier ridge model (EWRM) [8]. The angular correlation patterns of the alkaline-earth-metal atoms obtained using this method showed deviations from the He case. However, EWRM was unable to provide a rigorous analysis of these differences. Later on, a preliminary version of HRM-SOW was applied to Ca [9], confirming that this alkaline-earth-metal atom could show a behavior different from He. Yet the restriction of the treatment to the Wannier ridge precluded any definite conclusion. At this moment, in addition, no measurements were available against which theory could be tested. This is because unfortunately, alkaline earth-metal atoms are difficult to handle experimentally. The TDCSs for the direct DPI of the $4s^2$ valence shell of Ca were measured on a relative scale in 2000 [10] at an excess energy of 25.5 eV above the threshold. The two electrons were detected with equal energies in a plane perpendicular to the photon beam, one of them being ejected along the electric field of the linearly polarized light. However, the angular pattern obtained looked inconsistent with the expectations based on the widely used Gaussian model for the correlation factor. More recently, the direct DPI of the $2s^2$ valence shell of Be has been investigated experimentally and theoretically. The fully integrated cross section has been measured [11] and at the same time, but independently, it has been calculated using a CCC+model potential approach [12] and a TDCC+pseudopotential approach [13]. These two methods have also been used to predict singly and triply differential cross sections. All these experimental and theoretical results are in very reasonable agreement with each other. However, their respective interpretations lead to a rather muddled picture of the behavior of the escaping electron pair in Be compared to He, a topic that contributes importantly to the significance of these studies. It is therefore worth considering the Be DPI problem once more. This is done here by combining the HRM-SOW method with a model potential approach as explained in Sec. II. In Sec. III, we discuss the convergence conditions of the calculation in relation with the He case. Fully integrated cross sections are presented in Sec. IV and differential cross sections are in Sec. V, respectively. Special emphasis is put on the comparison between Be and He as well as on the comparison between the present work and the previous recent experimental and theoretical studies. Atomic units and radians are used everywhere unless otherwise stated.

II. GENERALIZATION OF THE HRM-SOW METHOD TO THE Be CASE

A. A short sketch of the HRM-SOW method

The HRM-SOW method [14,5,6] has been designed to deal with the one-photon ionization of two-electron systems above the double-ionization threshold. It allows to calculate the stationary state $\Phi_1(\vec{r}_1,\vec{r}_2)$ that is reached after photoabsorption by solving the stationary inhomogeneous equation

$$(\mathcal{H}_0-E)\Phi_1(\vec{r}_1,\vec{r}_2)=\Psi_G(\vec{r}_1,\vec{r}_2) \tag{1}$$

for outgoing waves boundary condition. $\mathcal{H}_0$ denotes the two-electron Hamiltonian of which $\Psi_0(\vec{r}_1,\vec{r}_2)$ is the ground-state wave function of energy E_0. E is the total energy of the system, that is related to E_0 by $E=E_0+\omega$, ω being the frequency of the incident light. The excess energy above the DPI threshold I^{2+} is shared between the two electrons according to $E-I^{2+}=E_1+E_2$, E_1, and E_2 being the energies of the two electrons. In what follows, we consider the plain case where the incident radiation is 100% linearly polarized, the study of which provides the sufficient basis for the treatment of more complex situations. The inhomogeneous term on the right-hand side, which acts as a source term, is then given by

$$\Psi_G(\vec{r}_1,\vec{r}_2)=-\frac{1}{2}(\vec{\mathcal{E}}_0\cdot\vec{D}_G)\Psi_0(\vec{r}_1,\vec{r}_2), \tag{2}$$

where $\vec{\mathcal{E}}_0$ is the amplitude of the electric field vector $\vec{\mathcal{E}}(t)=\vec{\mathcal{E}}_0\cos\omega t$, and $\vec{D}_G$ is the dipole operator, the expression of which is gauge dependent.

Equation (1) is solved using hyperspherical coordinates including the hyper-radius $R=\sqrt{r_1^2+r_2^2}$ and a set of five angles, denoted by Ω_5, that comprises: (i) the hyperangle $\alpha=\arctan(r_1/r_2)$, also referred to as the radial correlation angle, and (ii) the spherical angles $\Omega_1=(\vartheta_1,\varphi_1)$ and $\Omega_2=(\vartheta_2,\varphi_2)$ that specify the ejection directions of the two electrons in the laboratory frame with the z axis taken along the polarization direction. Note that, if only one radial distance, r_1 *or* r_2, tends towards infinity, which corresponds to single ionization, α tends towards $\pi/2$ *or* 0, respectively. But if both r_1 *and* r_2 tend towards infinity, which corresponds to DPI, then α tends towards a finite value related to the energy sharing between the two electrons, namely $\alpha\rightarrow\tan^{-1}(\sqrt{E_1/E_2})$.

To facilitate future explanations, let us introduce $\Phi(R;\Omega_5)=R^{5/2}\sin(2\alpha)\Phi_1(R;\Omega_5)$ and $\Phi^G(R;\Omega_5)=R^{5/2}\sin(2\alpha)\Psi^G(R;\Omega_5)$, and rewrite Eq. (1) more explicitly as

$$\left(-\frac{1}{2}\frac{\partial^2}{\partial R^2}+\frac{1}{2}\frac{\mathcal{T}(\Omega_5)}{R^2}-\frac{1}{8R^2}+\frac{\mathcal{V}(\Omega_5)}{R}-E\right)\Phi(R;\Omega_5)=\Phi^G(R;\Omega_5). \tag{3}$$

$\mathcal{T}(\Omega_5)$ is the angular kinetic-energy operator, given by

$$\mathcal{T}(\Omega_5)=-\frac{\partial^2}{\partial\alpha^2}+\frac{\ell_1^2}{(\sin\alpha)^2}+\frac{\ell_2^2}{(\cos\alpha)^2}, \tag{4}$$

ℓ_1^2 and ℓ_2^2 being the squared angular momenta associated with the two electrons. The three-body e-He^{2+}-e potential is written as the quotient of an angle-dependent effective charge $\mathcal{V}(\Omega_5)$ by the hyper-radius R, a form that emphasizes its Coulombic nature. The effective charge is given by

$$\mathcal{V}(\Omega_5)=-\frac{Z}{\cos\alpha}-\frac{Z}{\sin\alpha}+\frac{1}{\sqrt{1-\sin 2\alpha\cos\theta_{12}}}, \tag{5}$$

where Z is the nuclear charge and $\theta_{12}=\cos^{-1}(\vec{r}_1\cdot\vec{r}_2/r_1r_2)$ is the angle between the ejection directions of the two electrons, also referred to as the angular correlation angle. The resolution scheme is based upon partitioning the configuration space into two regions separated by the hypersurface defined by $R=R_0$.

We first extract the photoabsorption state $\Phi_1(R_0,\alpha;\Omega_1,\Omega_2)$ on this hypersurface using an $\mathcal{R}$-matrix approach that takes advantage of the properties of the adiabatic angular basis defined at $R=R_0$. In this process, we introduce the homogeneous counterpart of Eq. (3) that is made Hermitic over the finite inner region $R\leqslant R_0$ by adding the appropriate surface operator on the left-hand side. The main numerical task is then to compute the eigenvalues ϵ_k and eigenvectors Φ^k of the operator that figures on the left-hand side of this modified equation. To this end, we use a six-dimensional basis set comprising: (i) n_ℓ gerade and ungerade bipolar harmonics $\{{}^g\mathcal{Y}^{10}_{\ell,\ell+1}(\Omega_1,\Omega_2),{}^u\mathcal{Y}^{10}_{\ell,\ell+1}(\Omega_1,\Omega_2),\ell=0,1,\ldots,n_\ell-1\}$, respectively, symmetric and antisymmetric in the exchange of the two electrons, the angular momenta ℓ and $\ell+1$ of which are coupled to an $L=1$, $M=0$ resultant; (ii) n_α gerade and ungerade Fourier-type basis functions of period less than or equal to $\pi/2$ adapted to the boundary conditions that prevail within each ℓ subspace $\{{}^g\omega_n^\ell(\alpha)=(\sin\alpha\cos\alpha)^{\ell+1}\cos(4n\alpha),\quad n=0,\ldots,n_\alpha-1,\quad {}^u\omega_n^\ell(\alpha)=(\sin\alpha\cos\alpha)^\ell\sin(4n\alpha),\quad n=1,\ldots,n_\alpha\}$; and (iii) n_ρ Lagrange-Jacobi functions[1] which span the interval of variation [0,1] of the reduced hyper-radius $\rho=R/R_0$.

The second step, based on a semiclassical treatment of the R motion, consists of propagating the photoabsorption state from $R=R_0$ to $R=R_{\max}$ throughout the external region $R>R_0$. To this end, Φ_1 is expanded on n'_ℓ gerade and ungerade bipolar harmonics and on a n'_α-point α grid of variable stepsize that allows one to take proper account of the singular behavior of the potential in the vicinity of $\alpha=0$ and $\pi/2$.

One important feature of the method is that $\Phi_1(R,\alpha;\Omega_1,\Omega_2)$ is obtained over a hypersphere $R\leqslant R_{\max}$ of very large hyper-radius: typically, $R_{\max}\simeq 10^5$ to 10^6 a.u. This allows one to extract all single- and double-ionization cross sections directly from Φ_1 without relying upon approximate

[1]These functions were improperly referred to as Lagrange-Gegenbauer functions in Ref. [5].

asymptotic representations of the various continuum channels. This method being explained in detail in Refs. [5,6], we focus here on the modifications needed to pass on from *true* two-electron systems, such as He or its isoelectronic ions, to *quasi*-two-electron systems such as the alkaline-earths-metal atoms.

B. Alkaline-earth-metal atoms as quasi-two-electron systems

In alkaline-earth-metal atoms actually, the valence ns^2 orbital is well separated from the core orbitals on the coordinate scale as well as on the energy scale. This is well illustrated, in the Be case under study, by the very different radii of maximum charge density and the very different energies associated with the core and valence orbital in the Hartree-Fock (HF) limit [15]: $r_{1s} \simeq 0.14$ a.u. versus $r_{2s} \simeq 1.1$ a.u.; $\epsilon_{1s} \simeq -4.73$ a.u. versus $\epsilon_{2s} \simeq -0.31$ a.u. Accordingly, in many low-energy excitation processes, the core electrons are likely to behave as spectators, while the valence electrons are the actual performers. It is then natural to restrict the explicit treatment to the active valence electrons—the passive core electrons, which act as a polarizable electronic cloud shielding the nuclear charge, being described by an appropriate effective potential. Effective core potentials fall into two families.

Model potentials simulate the combined effect of the screened nuclear attraction and the core polarization. They are given usually by relatively simple analytic expressions depending on a few parameters. The latter are adjusted so that the resolution of the one-electron Schrödinger equation for the model potential yields eigenvalues in fair agreement with the valence and as many known excited levels of the (core + 1 electron) system as possible. Note that this optimization does not guarantee that the lowest eigenvalues of the one-electron Schrödinger equation give a correct representation of the core levels. Nor does it secure the accuracy of the valence and excited orbitals thoroughly: one should keep in mind that these orbitals are only bound to generate the correct energies and to present the correct number of nodes. Their accuracy has not been checked with respect to any other property.

Pseudopotentials, as compared with model potentials, incorporate one physical effect more, namely, the orthogonality of the valence orbitals to the core orbitals. They are obtained as the exact solutions of an *inverse problem* that allows some arbitrariness. Actually, a pseudopotential is defined to ensure that (i) the lowest eigenvalue of the associated one-electron Schrödinger equation coincides with the valence level of the (core + 1 electron) system; (ii) the associated nodeless orbital—called a *pseudo-orbital*—is identical with the true valence orbital in the valence region; and (iii) it has, in the complementary core region, some arbitrary smooth behavior chosen for computational convenience. The construction of pseudopotentials has been optimized from first principles, and the extended sets of them are now available for all atoms in the periodic system [16–18].

So, if model potentials and pseudopotentials both ''eliminate'' the core electrons in some sense, they do it to different extents. Pseudopotentials incorporate all the effects of the core electrons, including the associated orthogonality constraints, so that their elimination can be considered complete. The price to pay is that the behavior of the valence electrons in the core region is oversimplified, which is very likely to lead to gauge dependence in the calculation of electromagnetic transition rates. Conversely, model potentials do not prevent the electrons to collapse into the core. This leads to the appearance of superfluous, possibly unphysical states, sometimes referred to as virtual states. These states can be easily identified and eliminated. The only trouble with them is of a technical nature: their proper description may be numerically more demanding than that of the physical states of interest. But the definite advantage of model potentials is that they retain the complexity of the valence orbitals at short range. Accordingly, they are likely to preserve the gauge independence of the calculated photoionization cross sections. This has led us to choose a model potential approach.

Due to its simplicity, we have chosen for this first calculation the model potential derived by Bachau *et al.* [19], which takes the one-parameter local and central form

$$V_{\mathrm{m}}(r) = -\frac{(Z-N_c)}{r} - \frac{N_c}{r}(1+\gamma r)\exp(-2\gamma r), \qquad (6)$$

where $N_c = 2$ is the number of core electrons and $\gamma = 2.333\,710$ a.u. This potential modelizes the interaction between the valence electron and the doubly charged ionic core formed by the nucleus and the core electrons.

C. Modifications of HRM-SOW required in the Be case

Three formal modifications are then required to generalize the HRM-SOW method to the case of Be.

First, one has to replace the raw nuclear attraction $-Z/r_1 - Z/r_2$ by the screened nuclear attraction $V_{\mathrm{m}}(r_1) + V_{\mathrm{m}}(r_2)$ in $\mathcal{H}_0$ on the left-hand side of Eq. (1). This leads one to replace $\mathcal{V}(\underline{\Omega}_5)$ in Eq. (5) by a modified effective charge, denoted by $\overline{\mathcal{V}}(\Omega_5)$, which can be written from Eqs. (5) and (6) as

$$\begin{aligned}\overline{\mathcal{V}}(\Omega_5) = &-\frac{(Z-N_c)}{\cos\alpha} - \frac{(Z-N_c)}{\sin\alpha} + \frac{1}{\sqrt{1-\sin 2\alpha\cos\theta_{12}}} \\ &- N_c\left(\frac{\exp(-2\gamma R\cos\alpha)}{\cos\alpha} + \frac{\exp(-2\gamma R\sin\alpha)}{\sin\alpha}\right) \\ &- N_c\gamma R[\exp(-2\,\gamma R\cos\alpha) + \exp(-2\gamma R\sin\alpha)].\end{aligned} \qquad (7)$$

The calculation of the matrix elements of the additional terms that appear above in the basis set presented in Sec. II A does not present any special difficulty.

Second, one has to replace the Hylleraas-type ground-state wave function $\Psi_0(\vec{r}_1,\vec{r}_2)$ of He on the right-hand side of Eq. (2) by a two-electron ground-state wave function of Be, consistent with the model potential chosen.

We have calculated this *valence-only* ground-state wave function of Be by the configuration interaction (CI) method.

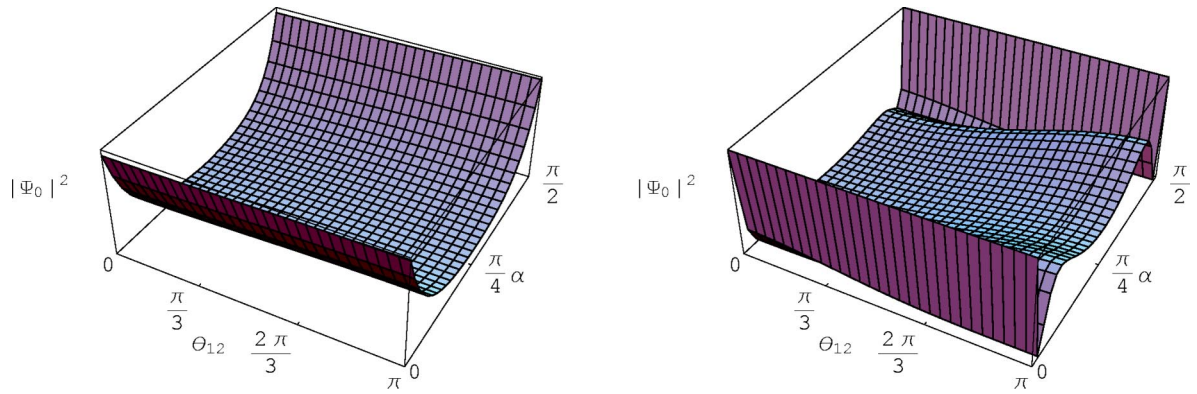

FIG. 1. Surface plots of the squared modulus (in a.u.) of the ^1S ground-state wave function of He (left plot) and of the ^1S valence-only ground-state wave function of Be (right plot) at $R=1.5$ a.u. and $R=5$ a.u., respectively. The radial and angular correlation angles are given in radians.

The two-electron ^1S configuration state functions included in the CI expansion are built from the valence and excited orbitals of the one-electron Hamiltonian associated with the potential $V_m(r)$. The exclusion of the core-type virtual orbital $\overline{1s}$ prevents any collapse of the two-electron wave function to the core. The monoelectronic orbitals are computed using the Lagrange-mesh technique. Accordingly, the radial orbitals are expanded on a basis of N Lagrange-Laguerre functions and the radial coordinate is scaled by a parameter $h=2r_{\max}/(x_N+x_{N+1})$ chosen to ensure that the set of scaled knots $hx_1, hx_2, \ldots, hx_N$ of the Laguerre mesh spans the interval $[0,r_{\max}]$ adequately. The matrix elements are calculated using the Gauss quadrature associated with the Lagrange-mesh. They are given accordingly by compact analytical formulas involving the values of the potential at the scaled knots, the values of the knots themselves, and the dimension of the mesh. All details of the numerical approach are given in Ref. [20] in the illustrative case of Ca. Here, using $r_{\max}=15$, $N=20$, and a full CI including orbitals from $\ell=0$ to $\ell=6$, we have obtained a two-electron ground-state wave function of Be, the energy E_0 of which—measured with respect to the Be^{2+} ground-state—is -1.0128 a.u., compared to the experimental value of -1.0115 a.u. [21].

A surface plot of the squared modulus of this wave function at $R=5$ a.u. $\simeq 5\, r_{2s}$(Be) as a function of θ_{12} and α is given in Fig. 1. It shows more pronounced structures with respect to these angular and radial correlation angles than its He counterpart plotted besides for $R=1.5$ a.u. $\simeq 5\, r_{1s}$(He). This is a graphical illustration of the increased importance of electronic correlations in the $2s$ valence shell of Be compared to the $1s$ valence shell of He.

The ratio $E_0^c/E_0=1-E_0^{\mathrm{HF}}/E_0$ is another, global, measure of the strength of these correlations. In this ratio, E_0^c is the correlation energy of the valence electron pair, defined as the difference between its total energy E_0 and the HF approximation E_0^{HF} of the latter, all energies being defined with respect to the double-ionization limit. This ratio can be evaluated at 1.4% for He and at 4.6% for Be from Refs. [15,21,22]. According to this estimate, correlations in the valence electron pair are then about three times more effective in Be than in He. We shall see soon that these differences in the initial states of the electron pair will affect the DPI cross sections significantly.

The third and last modifications required concern the expression of the dipole operator in the acceleration gauge. The latter indeed is given in full generality [23] by

$$\vec{D}_A=\frac{1}{2\omega^2}(\vec{\nabla}_1 V+\vec{\nabla}_2 V), \tag{8}$$

where V is the potential experienced by any electron in the pair, while the other is away. This potential is the pure Coulombic potential $-Z/r$ for He, but for Be, it is the model potential $V_m(r)$. The R^{-2} scaling of $\vec{D}_A$ observed in He thus disappears in Be. So does the common idea that the acceleration gauge given by Eq. (8), compared with the velocity gauge

$$\vec{D}_V=\frac{1}{\omega}(\vec{\nabla}_1+\vec{\nabla}_2), \tag{9}$$

"zooms" on a region of space closer to the nucleus. The respective actions of the two operators on the initial-state wave function yet remain very different, one involving the product of the wave function by the gradient of the potential, and the other the gradient of the wave function itself. The use of both in parallel thus constitutes a significant check of the numerical accuracy of the calculation.

III. CONVERGENCE OF THE CALCULATION IN Be COMPARED TO He

Once the three modifications discussed above have been implemented, the DPI calculation proceeds as in He. However, a comparison of the three-body potentials involved in the Be case and in the He case leads one to anticipate different convergence conditions of the calculation for these two atoms. Figure 2 shows cuts of these e-He^{2+}-e and e-Be^{2+}-e potentials $\mathcal{V}(\Omega_5)/R$ and $\overline{\mathcal{V}}(\Omega_5)/R$ along $\theta_{12}=\pi$, for various values of R, as a function of α. As these potentials are symmetric with respect to $\alpha=\pi/4$, we restrict their representation to the α interval $[0,\pi/4]$ on the left plot. Clearly, the

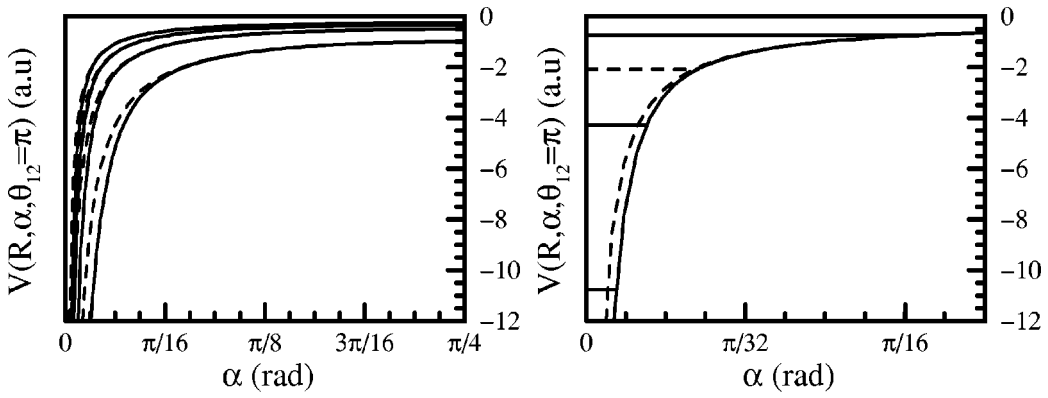

FIG. 2. Cuts of the three-body potential surfaces associated with Be (solid lines) and He (dashed lines) along $\theta_{12}=\pi$ for $R=5$, 10, 15, and 20 a.u. from bottom to top on the left plot, and for $R=15$ a.u. on the right plot. The horizontal segments on the right plot indicate the positions of the deepest adiabatic levels in Be (solid lines) and in He (dashed line).

two potentials coincide on an α interval, centered at $\pi/4$, the width of which increases as R increases. Conversely, the Be potential appears as much more attractive than the He one within two α intervals, located about $\alpha=0$ and $\pi/2$, the widths of which decrease as R increases. For R equal to the hyper-radius $R_0=r_{\max}=15$ a.u. of the inner region used in the present HRM-SOW calculation, the two potentials depart from each other only in two intervals of width of 0.067 rad about $\alpha=0$ and $\pi/2$ (see right plot).

This α interval where He and Be can be distinguished shrinks as R increases. Moreover, the wave functions of the electron pair scale as $\alpha^{\ell+1}$ and $(\pi/2-\alpha)^{\ell+1}$ in the vicinity of $\alpha=0$ and $\pi/2$ respectively, ℓ being the angular momentum of one electron. So, as R increases from R_0, the escaping electron pair becomes rapidly insensitive to the differences between the two cores left behind. This is why the *external region* calculation converges for the same parameters in Be and He, namely $n'_\ell=25, n'_\alpha=1000, R_{\max}=10^4$ to 10^6 for excess energies above the threshold ranging from a few tens of eV to a few eV.

By contrast, the differences between the two targets do modify the *inner region* calculation. They do not affect the size of the Lagrange-Jacobi mesh used to describe the reduced hyper-radius $\rho=R/R_0$ nor the number of one-electron angular momenta required, which are given by $n_\rho=23$, for $R_0=15$ a.u., and $n_\ell=5$, respectively. But they influence the number of Fourier-type α-basis functions, which has to be increased significantly, namely from about $n_\alpha=40$ for He to about $n_\alpha=60$ for Be. This is not surprising since the slope of the potential with respect to α is larger in Be than in He by about a factor of 2 in the singular regions around $\alpha=0$ and $\pi/2$.

Another way to look at these different computational requirements of He and Be is to consider the adiabatic energies computed on the hypersurface $R=R_0=15$ a.u. in both cases. These adiabatic energies are solutions of the eigenvalue equation deduced from Eq. (3) by suppressing the inhomogeneous term and the partial derivative with respect to R and setting $R=R_0$. They can be viewed as bound levels in the potential wells $\mathcal{V}(\Omega_5)/R_0$ and $\overline{\mathcal{V}}(\Omega_5)/R_0$ at $R_0=15$ a.u. Their positions are represented on the right plot of Fig. 2 where cuts of these potential surfaces along $\theta_{12}=\pi$ are available. In He, the lowest adiabatic level, which corresponds to the system formed by one electron a distance R_0 away from He^+ in its ground-state, lies at -2.07 a.u. Figure 2 shows that the associated state extends over a region of about 0.067-rad wide in α at $\theta_{12}=\pi$. In Be, the three lowest adiabatic states lie at -10.76, -4.27, and -0.73 a.u., respectively, their associated α widths at $\theta_{12}=\pi$ being 0.02, 0.04, and 0.2 rad.. The lowest two are non physical virtual states resulting from the use of a model potential that does not prevent the collapse of any of the two electrons to the core. The third is the one that can be interpreted physically as corresponding to one electron a distance R_0 away from Be^+ in its ground-state. The appearance of compact tightly bound virtual states makes the inner region $\mathcal{R}$-matrix treatment more demanding numerically. Actually, the nth function in our α-basis set has a period $\tau_\alpha^n=\pi/2n$ which equals 0.039 rad for $n=40$. This is clearly adequate for describing the lowest adiabatic state in He, that extends over about 0.067 rad, but not the lowest one in Be, since it is only 0.02-rad wide in α. One understands easily that $n=60$, yielding $\tau_\alpha^{60}=0.026$ rad, is more appropriate.

Before closing these technical considerations, let us come back to the number of one-electron angular momenta included. It was pointed out in Refs. [12,13] that more partial waves were needed in Be than in He in order to obtain converged TDCSs using the CCC and TDCC methods: namely, $n_\ell=7$ was required in Be while $n_\ell=4$ had proved enough for He. We have checked here that increasing n_ℓ from 5 to 7 in the inner region while keeping $n'_\ell=25$ in the external region has no significant effect on the TDCSs obtained using the HRM-SOW approach. There is in fact no contradiction between these apparently opposite remarks. Actually, in CCC and TDCC, the numerical calculation involves a unique region of space that extends over about 100 a.u. In HRM-SOW, by contrast, two different regions are considered, a small inner region of 15 a.u. extension, and a very large complementary outer region that reaches distances of the order of 10^6 a.u. It is therefore not surprising that the number of partial waves needed in CCC and TDCC ($n_\ell=7$) is bracketed by those used in HRM-SOW in the inner region

($n_\ell = 5$) and in the outer region ($n'_\ell = 25$), respectively. This only indicates that this number increases with the size of the system. This is consistent with the fact that for infinite mutual distances of the three particles, the two electrons will behave as free particles associated with plane waves, the partial-wave expansion of which involves an infinite number of terms.

IV. FULLY INTEGRATED CROSS SECTIONS

The analysis of the wave function at R_0 into adiabatic components has already been considered in Sec. III. Its main features, in the Be case, are the following: (i) the two lowest components, denoted by $\Phi_1^\lambda, \lambda = 1,2$, are related to single ionization to unphysical virtual states of the ion that appear due to the use of a model potential; (ii) the third component Φ_1^3 is associated with single ionization to the ground state of the ion; (iii) the identification of adiabatic components with virtual or physical outgoing channels of the photoabsorption process cannot be pushed further since the remaining channels, namely, single ionization with excitation and double ionization, are still tightly coupled together at R_0. Let us now introduce $\overline{\Phi_1^\lambda} = \Phi_1 - \Sigma_{\mu=1}^{\lambda} \Phi_1^\mu$. Following the analysis reminded above, the fully integrated cross section (ICS) for total (single + double) ionization can be deduced from the flux of $\overline{\Phi_1^2}$ through the hypersurface $R = R_0$, the ICS for single ionization without excitation from the flux of Φ_1^3 through this same hypersurface, and we have to propagate $\overline{\Phi_1^3}$ from R_0 to $R_{\max}$, before we can extract the various cross sections associated with all other excitation and/or ionization processes. The DPI cross sections, in particular, will be extracted from the flux of the propagated wave function through the hypersurface $R = R_{\max}$ for $\alpha \neq 0, \pi/2$.

A. Total photoionization

The top plot of Fig. 3 shows the total (single+double) photoionization ICS from 2 to 53 eV above the double-ionization threshold. The present calculations in the velocity *V* and acceleration *A* gauges cannot be distinguished from each other at the scale of the figure. They agree well with the corresponding length *L* calculation, that lies sligthly higher, the more so the lower the energy, and with the only set of measurements available [11]. Note that the latter is not absolute: it is deduced from measurements of the double to single photoionization ratio using the absolute scale provided by previous calculations of the single photoionization ICS [24,25]. CCC calculations [12] have also been performed in a model potential approach where the $1s^2$ core is supposed to be frozen in the HF ground state of Be^{2+} [26]. The valence-only wave function of the Be ground-state is then computed in a MCHF (multiconfigurational Hartree-Fock) approximation. The CCC results in the *L* gauge lie very close to our *V* and *A* curves, although sligthly below. The CCC curve in the *V* gauge lies still a bit lower. The behavior of the two methods with respect to a change of gauge is very similar: the results are little altered, with the *L*-gauge calculation leading to a higher total cross section, especially on the low-energy side. The differences between the two methods can be attributed to the different modelizations of the core used in each case.

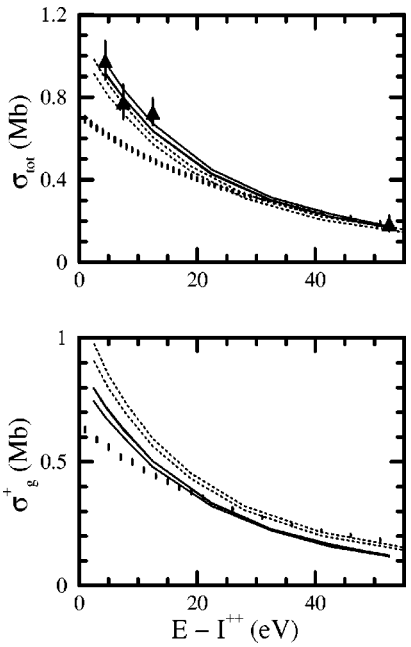

FIG. 3. Top, total photoionization cross section, in Mb, as a function of the excess energy above the double-ionization threshold in eV. Triangles with error bars, measurements on Be [11]; solid lines, HRM-SOW calculations on Be in the *L*, *V*, and *A* gauges (see text); dotted lines, CCC calculations on Be in the *L* and *V* gauges (see text); small dots with error bars, measurements on He [27]. Bottom, single-photoionization cross section to the ground state of the ion, in Mb, as a function of the excess energy above the double-ionization threshold in eV. Solid lines, HRM-SOW calculations on Be in the *L*, *V*, and *A* gauges; dotted lines, CCC calculations in the *L* and *V* gauges; small dots with error bars, measurements [28] on He.

B. Single ionization without excitation

This cross section is displayed on the bottom plot of Fig. 3 in the same 2–53 eV energy range above the DPI threshold as before. The *L* and *V* calculations cannot be distinguished at the scale of the figure, while the A calculation lies a bit lower. No measurements are available for this quantity, but CCC calculations have been performed, which are given in the *L* (upper curve) and *V* (lower curve) form. This plot provides additional evidence of a similar behavior of the two sets of calculations with respect to a change of gauge. However, the CCC approach predicts a higher single ionization without excitation cross section than the present approach, while it predicted a slightly lower total ionization cross section. These disagreements will add to each other when the total DPI cross section will be considered.

C. Double photoionization

The ICS for DPI is represented on Fig. 4 along with the only measurement available [11] and the most recent calculations [12,13]. In the TDCC calculation, a homemade pseudopotential is used, which forbids any reasonable de-

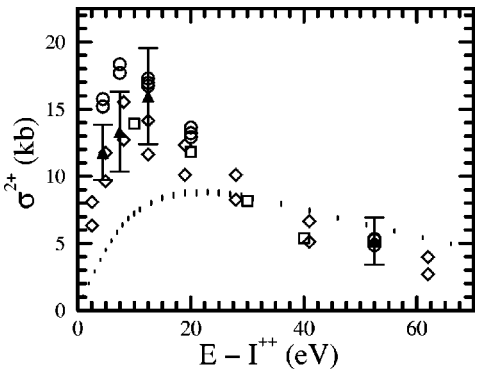

FIG. 4. Total DPI cross section, in kb, as a function of the excess energy above the DPI threshold, in eV. Full triangles with errors bars, Be measurements [11]; empty circles, HRM-SOW calculations on Be in the *L*, *V*, and *A* gauges; empty diamonds, CCC calculations on Be in the *L* and *V* gauges [12]; empty squares, TDCC calculation on Be in the *L* gauge [13]; small dots with error bars, He measurements [29].

scription of the short range dynamics. Accordingly, the results are presented only in the *L* gauge. The CCC calculations, based on a frozen core model potential, are available in the *L* and *V* gauges, and the present HRM-SOW calculations, which rely upon an empirically adjusted model potential, in the *L*, *V*, and *A* gauges.

The present calculations show a very weak gauge dependence. They fall *within* the experimental errors bars at the two highest energies where the cross section has been measured but *above* these error bars at the two lowest energies. A similar overestimation of the DPI cross section by the HRM-SOW method was observed before in He below 5 eV [5]. It probably reflects a limitation of the present implementation of the HRM-SOW method, which does not allow to increase the size of the inner region up to the values that would be needed at very low energies. Progress is being done in this respect at the moment. The CCC calculations show a more pronounced gauge dependence than the present ones. They were not performed at the experimental energies, yet a quick by-eye interpolation shows that the segment which connects the *L* result to the corresponding *V* one would overlap the experimental error bars at all measured energies. The TDCC results also look consistent with the experimental data and the CCC calculations in the restricted 10–40 eV range where they are available. It is not possible to locate the maximum of the cross section precisely based on the present data. From the experimental points, one would locate it above 12.5 eV, and, from both the CCC and HRM-SOW calculations, between 7.5 and 12.5 eV. No estimate of the position of the maximum can be obtained from TDCC due to the lack of points on the low-energy side.

It is worth observing that the scattering of the various calculations available is of the same order of magnitude as the experimental error bars. This can be considered satisfying by giving the very different treatments used in each case.

D. He compared to Be

Figures 3 and 4 also contain the experimental ICSs measured for He with respect to the excess energy above the He DPI threshold [27–29]. They display the same overall behavior as their Be counterparts. However, on the three figures, the He curves lie below the Be ones at low energy, come closer to them as energy increases, and finally seem to cross them at the upper bound of the energy interval studied. We have seen already in Sec. III that the potential experienced by the outgoing electron pair is the same for He and Be at large *R*. The differences pointed out above between the He and Be ICSs then originate in the small *R* region to which we focus now.

A few eV from the threshold, the energy *E* is negligible with respect to both the e-He^{2+}-e and the e-Be^{2+}-e three-body potentials that govern the motion of the escaping electrons at small *R*. As a result, the outgoing electron pair does not distinguish between the two ions left behind. The differences observed between the He and Be ICSs should then derive from the different characteristics of the initial states. In this respect, one important feature of the Be ground-state is that it is much more diffusive than the He ground state, which should result in a better overlap with the final single or double continuum state. This could explain why the Be ICSs dominate the He ICSs at low energy in each of the three channels considered, be it total ionization, single ionization without excitation, or double ionization. Another characteristic of the initial state plays a role in the DPI channel. Actually, DPI being boosted by the electronic correlations in the initial state, the initial state's more correlated structure of Be compared to He (see Sec. II) might also contribute to the increase of the DPI ICS observed in Be with respect to He in this low-energy range.

At a few tens of eV above the threshold, by contrast, the energy *E* becomes comparable in magnitude to the three-body potentials that determine the dynamics of the electron pair at small *R*. Accordingly, the two electrons feel the stronger attraction of the Be core compared to the He nucleus, which makes the single or double escape more difficult for Be. The higher ICSs observed in He with respect to Be on the high-energy side then reveals that, far from the threshold, this final-state effect predominates over the initial-state effects discussed just above.

V. DIFFERENTIAL CROSS SECTIONS

For the time being, no measurements have been made of the differential DPI cross sections of Be. Only theoretical calculations are available [12,13], which have been performed at 20 eV above the threshold, for the sake of comparison with the numerous He data obtained at this energy. Whether this energy is the most likely to be studied in future differential experiments on Be is not completely clear: on one side, it does not correspond to the expected maximum of the DPI ICS for Be, although it does so for He; but on the other side, the detection of the ionized electrons is all the more easy the higher their energy. As a result, we have chosen to favor the possibility of comparing our data with those of other theories and with the He measurements, and we present below a set of Be DPI differential cross sections obtained at this excess energy of 20 eV.

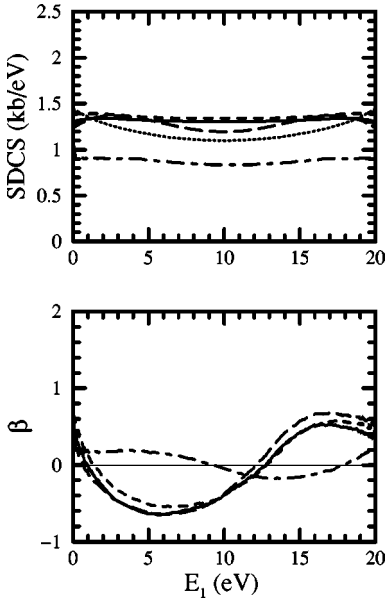

FIG. 5. Top, singly differential DPI cross section in kb/eV versus the energy of one electron in eV. Solid line, HRM-SOW calculation for Be in the *L* gauge; dashed line, same in the *V* gauge; long-dashed line, same in the *A* gauge; dotted line, TDCC calculation for Be in the *L* gauge [13]; dashed-dotted line, HRM-SOW calculation for He [5]. Bottom, dimensionless β parameter for the doubly differential DPI cross section versus the energy of one electron in eV. Solid line, HRM-SOW calculation for Be in the *L* gauge; dashed line, same in the *V* gauge; long-dashed line, same in the *A* gauge; dashed-dotted line, HRM-SOW calculation for He [5].

A. SDCS

The singly differential cross section (SDCS) presented at the top of Fig. 5 informs one about the sharing of the energy between the two electrons. The gauge dependence of the HRM-SOW results is weak. Only does the A-gauge curve show more pronounced oscillations than the *V*- and *L*-gauge ones, which are almost flat, as in the He case that is also represented for the record. The *L*-gauge TDCC [13] result lies a bit lower, as expected from the lower ICS obtained using this method (see Fig. 4). It also has a different shape, that looks like parabolic, with a relatively pronounced concavity. This is clearly different from the shapes obtained from HRM-SOW, accurate fits of which cannot be obtained usually with polynomials of degree less than 6.

B. DDCS

The doubly differential cross section (DDCS) can be expressed in terms of the SDCS and the dimensionless asymmetry parameter $\beta(E_1,E_2)$ [see Eq. (40) of [5]]. The DDCS being positive, β ranges from -1 to $+2$. The value $+2$ yields, for the only electron detected, a $\cos^2\vartheta_1$ angular distribution which favors emission along the electric field. The value 0 provides an isotropic distribution. The value -1 leads to a $\sin^2\vartheta_1$ distribution where the emission occurs preferentially in the direction perpendicular to the electric field. This is a manifestation of the electronic correlations which prevent the electrons from simply following the external field. As for the SDCSs seen above, the gauge dependence of the Be β parameters obtained from HRM-SOW is weak (see the bottom of Fig. 5). Compared to the He β parameter, that never departs markedly from zero, the Be β parameter shows much larger variations with respect to the energy sharing. The minimum value of β is -0.6 for Be compared to -0.2 for He, which indicates that stronger electronic correlations can be observed in Be. The β parameter thus allows one to estimate the relative strength of correlations in multielectronic systems, which is a valuable information, without calling upon sophisticated coincidence techniques. Despite these advantages, it has only rarely been considered by experimentalists. We hope that the present results will be a stimulus for future measurements.

C. TDCS

The TDCSs we present now have been obtained assuming linear polarization. Their dependence upon the experimentally measured quantities—energies and angles referred to the laboratory frame, is enlightened by the well-known expression

$$\frac{d^3\sigma}{d\Omega_1 d\Omega_2 dE_1} = |\mathcal{A}_g(E_1,E_2,\theta_{12})(\cos\vartheta_1+\cos\vartheta_2) + \mathcal{A}_u(E_1,E_2,\theta_{12})(\cos\vartheta_1-\cos\vartheta_2)|^2, \tag{10}$$

derived by Huetz and co-workers [30], where geometric and dynamic factors are separated conveniently, completed by the geometric relation

$$\cos\theta_{12}=\cos\vartheta_1\cos\vartheta_2+\sin\vartheta_1\sin\vartheta_2\cos\varphi \quad \text{with}$$

$$\varphi=\varphi_1-\varphi_2. \tag{11}$$

The gerade and ungerade complex amplitudes $\mathcal{A}_g(E_1,E_2,\theta_{12})$ and $\mathcal{A}_u(E_1,E_2,\theta_{12})$ are, respectively, even and odd in the exchange of the two electrons, which reduces here to the exchange of their energies, since θ_{12}, defined over $[0,\pi]$, is invariant in this operation. They contain all the dynamic information about the system. Their dependence on the energy ratio E_1/E_2 is a manifestation of the radial correlations in the electronic pair. It is worth noting that the ungerade component vanishes at equal energy sharing leading to a very simple expression of the observed TDCS. The two amplitudes have a maximum at $\theta_{12}=\pi$ and cancel down to zero at $\theta_{12}=0$, which reflects the effect of the electronic angular correlations that push the ejection directions of the two electrons away from each other. Actually, the width of the θ_{12} interval where these amplitudes have a significant magnitude is related to the strength of angular correlations: the wider this width, the weaker the angular correlations. Much efforts have been invested accordingly to quantify this qualitative picture [31]. They have proved particularly successful as to the gerade amplitude that is of special importance, since it is the dominant amplitude in most cases, and the only contributing one at equal-energy sharing. It has been

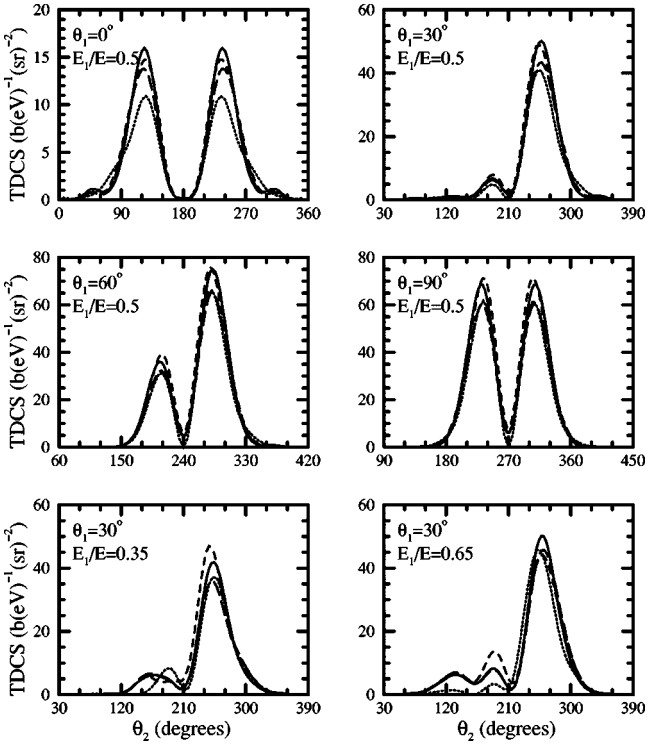

FIG. 6. TDCSs for the direct DPI of Be at 20 eV above threshold in b/eV/(sr)^2. Linear polarization and perpendicular geometry are assumed (see text). Solid lines, HRM-SOW calculation in the *L* gauge; dashed line, same in the *V* gauge; long-dashed line, same in the *A* gauge; dotted line, TDCC calculation in the *L* gauge [13].

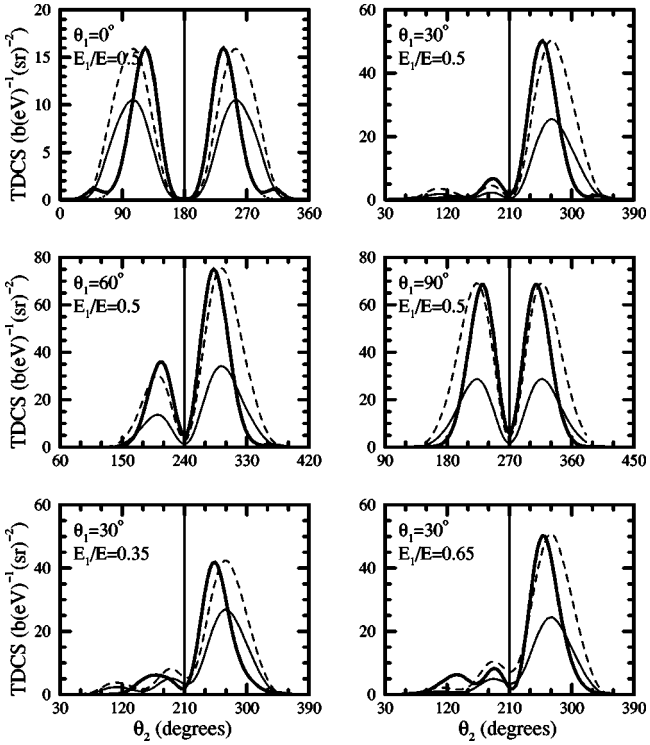

FIG. 7. TDCSs for the direct DPI of Be and He at 20 eV above threshold in b/eV/(sr)^2. Linear polarization and perpendicular geometry are assumed (see text). Thick solid lines, HRM-SOW calculation in the *L* gauge for Be; thin solid lines, same as before but for He; thin dashed line, same as before but rescaled to the Be peaks; thin dotted line on the top left plot, Gaussian ansatz (see text).

shown indeed that the θ_{12} dependence of $|\mathcal{A}_g|^2$ can be effectively approximated by the Gaussian form

$$|\mathcal{A}_g(E_1,E_2,\theta_{12})|^2 = a_g(E_1,E_2)\exp\left(-\frac{4\ln 2(\theta_{12}-\pi)^2}{\Gamma^2(E_1,E_2)}\right) \tag{12}$$

that depends on two parameters: an overall scaling factor a_g that is not of much interest to us here, and the width Γ, which provides us with the expected quantitative measure of the strength of angular correlations. Both these parameters are usually assumed to be independent of the energy sharing.

The TDCS presented in Figs. 6 and 7 have been obtained from Eq. (10) using the $\mathcal{A}_g$ and $\mathcal{A}_u$ amplitudes that are extracted directly from the HRM-SOW wave function obtained at R_{max}. They have been averaged over the ϑ_1, ϑ_2, and φ angular sectors over which the experimental He data were accumulated in Ref. [1], as was done with previously computed He TDCSs, in order to make the comparison between He and Be as relevant as possible. As a result of this averaging process, the exact nodes that are expected for antiparallel emission at equal energy sharing are partly smeared.

Complementarily, Eqs. (10) and (12) have been adjusted to the computed equal energy sharing TDCS at $\vartheta_1 = 0°$ in order to extract the empirical width parameter Γ for the sake of comparison with the value reported in Ref. [12].

Figure 6 shows a set of TDCSs obtained for various energy sharings, characterized by $E_1/E = 0.35$, 0.5, and 0.65, respectively. The two electrons are emitted in the plane perpendicular to the linearly polarized photon beam (perpendicular geometry), and one of them is ejected at various angles from the electric field, ranging from $\vartheta_1 = 0$ to 30, 60, and 90°. This series of graphs thus covers a wide range of different dynamic situations. The *L*, *V*, and *A*-gauge HRM-SOW calculations are represented along with the *L*-gauge TDCC calculation. At equal energy sharing, the effect of a change of gauge reduces essentially to a rescaling of the HRM-SOW TDCSs by 15% at most. Conversely, at unequal energy sharing, the change of gauge has more significant consequences, since it modifies the shapes of the secondary structures and alters the height of the main peak by as much as 25% when $E_1/E = 0.35$. The overall agreement between the HRM-SOW and TDCC calculations is quite reasonable. They depart from each other more markedly for equal energy sharing at $\vartheta_1 = 0°$, where the heights of the peaks differ by as much as 30%, and for unequal energy sharings where the secondary structures take different shapes and magnitudes. This confirms that these two kinematics are particularly sensitive test cases for the theory as already noted in Ref. [6].

Figure 7 illustrates the same dynamic situations as Fig. 6 but the TDCSs depicted correspond now to Be and He treated in the *L*-gauge HRM-SOW approach. The He TDCSs appear systematically smaller than the Be ones, by factors that range from about 0.4 to about 0.65. This is consistent

with the ratio $\sigma^{2+}(\mathrm{He})/\sigma^{2+}(\mathrm{Be}) \simeq 0.66$ of the computed ICSs that can be estimated from Fig. 4 of this paper and from Fig. 5 of Ref. [5]. The He TDCSs display the same overall shape as the Be ones. The small differences are better appreciated by comparing the Be TDCSs with the He ones rescaled by the ratio of the Be peaks to the He ones. The abscissa corresponding to $\vartheta_2 = \vartheta_1 + \pi$ is emphasized by a vertical line. As announced above, the extension of the TDCSs away from this line is an inverse measure of the strength of the electronic correlations. A quick glance at Fig. 7 thus convinces one that the effect of electronic correlations is more important in Be. If we put the Gaussian ansatz of Eq. (12) with $\Gamma = 68°$ and $a_g = 540$ into Eq. (10), we obtain an empirical TDCS that coincides with the *ab initio* computed one everywhere but in the large-θ_{12} wings, as can be seen by careful inspection of the top-left plot of Fig. 7. This value of Γ is in excellent agreement with the value reported in Ref. [12]. It is significantly lower than the corresponding 91° value obtained for He at the very close energy of 18.6 eV [32]. This supports the conclusion already set forth above and in [12] that electron correlation effects are significantly stronger in Be than in He. Note that Fig. (4) of Ref. [13] evidences the agreement between TDCC and CCC calculations. This implies that the TDCC calculations support the above conclusion too—despite inappropriate comments by the authors focusing on the similarities between the two targets.

VI. CONCLUSION

We have presented the first nonrestrictive HRM-SOW calculation of the DPI of an alkaline earth-metal atom, namely, Be. Fully integrated, singly, doubly, and triply differential cross sections are shown, which exhibit only a weak gauge dependence. The calculated ICSs are sligthly too large at the two lowest energies where the measurements have been performed [11], yet they fall within the experimental error bars at higher energies. The entire set of computed cross sections is in reasonable agreement with the other recent theoretical data [12,13]. This agreement is all the more remarkable the more different the different theories used: CCC, TDCC, and HRM-SOW which have little in common indeed beyond the use of the same four-dimensional basis of bipolar harmonics. Moreover, the valence-only descriptions of Be are also very different in each case: the effective core potential is a home made pseudopotential in TDCC, a frozen-core HF potential in CCC, and an empirically adjusted model potential taken from the literature in HRM-SOW. Also, the valence-only ground-state wave functions of Be that enter the various calculations result from very different computational schemes: relaxation in imaginary times on a two-dimensional radial grid in TDCC, MCHF in CCC, CI in HRM-SOW—and they lead to ground-state energies of different accuracies lying within 10^{-2} a.u. of the experimental value in TDCC and within 10^{-3} a.u. in HRM-SOW, for instance. The relative stability of the DPI results with respect to such important variations in the computational approaches, as well as with respect to the change of gauge in the HRM-SOW and CCC cases, gives credit to the resulting picture of Be, which appears as a more correlated two-electron system than He.

It is likely that the interest of experimentalists in alkaline-earth metals will be boosted by these very promising calculations. The systematic study of the direct DPI process through the second column of the periodic table therefore seems to be very much in the news. As one important motivation for such a study is to follow the evolution of the correlations in the electron pair as the size of the system increases, we believe that some thinking is needed regarding the definition and characterization of electronic correlations in the continuum. The Appendix below is an attempt to initiate a debate on this subject.

ACKNOWLEDGMENTS

We thank J. Colgan and A. Kheifets for communicating their data files to us. The LIXAM members acknowledge the support of the CNRS computer center IDRIS (Orsay, France) through Project No. 021485. A.K.K. acknowledges the financial support of the Russian Foundation for Fundamental Research via Grant No. 02-02-16586.

APPENDIX: ELECTRONIC INTERACTIONS AND ELECTRONIC CORRELATIONS

The term of electron-electron correlations embodies all physical effects occuring in multielectron systems and that cannot be described within the independent-particle HF approximation. They cannot be identified with any specific term in the multielectron Hamiltonian, and, in particular, they cannot be identified with the electron-electron interaction term $\Sigma_{i<j} r_{ij}^{-1}$. To get the proper picture of the relation between these two notions one has to remind oneself that the HF approximation takes a full account of the electron-nuclei interaction and a large but incomplete account of the electron-electron interactions. Electron-electron correlation effects can thus be viewed as those effects of the electron-electron interactions that baffle any independent-particle description.

The next problem is how to estimate electronic correlations quantitatively.

The answer is clear for bound states where the correlation energy, defined as the difference between the total energy and its HF approximation, provides a global measure of these effects. It was used in Sec. II to characterize the strength of correlations in the initial states of He and Be. Note in passing that the effect of correlations is to lower the total energy with respect to the HF limit by minimizing the electron-electron repulsion, so that strong correlations mean weak electron-electron interactions.

The correlation energy introduced above cannot be defined for continuum states. One could then consider the DPI ICS σ^{2+}, which is well known to be particularly sensitive to correlations, as an alternative candidate. However, the measure provided would be biased by the sensitivity of this quantity to the correlations in the initial bound state. The double to single photoionization ratio σ^{2+}/σ^{+}, that is sensitive to other effects than the correlation ones due to the

presence of the single-ionization cross section, *a fortiori* does not provide a proper alternative either. The quantities which are used here to characterize correlations in the continuum are the dependences of the wave function on the collective variables α and θ_{12}. They can be used in bound states as well. This approach is consistent with the physical intuition. It is also well established by common practice, as evidenced by the current characterization of α and θ_{12} as *radial and angular correlation angles*, respectively, and by the use of the width parameter Γ to evaluate angular correlations quantitatively. Yet we acknowledge that this measure of the correlations has never received fully satisfying formal justifications. To our knowledge indeed, a *mathematically rigorous and physically convenient* characterization of a two-electron independent particle wave function, or, conversely, of a two-electron correlated wave function, is still lacking.

[1] H. Bräuning, R. Dörner, C.L. Cocke, M.H. Prior, B. Krässig, A.S. Kheifets, I. Bray, A. Bräuning-Demian, K. Carnes, S. Dreuil, V. Mergel, P. Richard, J. Ullrich, and H. Schmidt-Böcking, J. Phys. B **31**, 5149 (1998).

[2] A. Huetz and J. Mazeau, Phys. Rev. Lett. **85**, 530 (2000).

[3] M. Achler, V. Mergel, L. Spielberger, R. Dörner, Y. Azuma, and H. Schmidt-Böcking, J. Phys. B **34**, 965 (2001).

[4] J. Colgan, M.S. Pindzola, and F. Robicheaux, J. Phys. B **34**, L457 (2001).

[5] P. Selles, L. Malegat, and A.K. Kazansky, Phys. Rev. A **65**, 032711 (2002).

[6] L. Malegat, P. Selles, and A.K. Kazansky, in *Many-Particle Quantum Dynamics in Atomic and Molecular Fragmentation*, edited by J. Ullrich and V. P. Shevelko (Springer, Heidelberg, in press).

[7] S.C. Ceraulo, R.M. Stehman, and R.S. Berry, Phys. Rev. A **49**, 1730 (1994).

[8] A.K. Kazansky and V.N. Ostrovsky, J. Phys. B **30**, L835 (1997).

[9] L. Malegat, F. Citrini, P. Selles, and P. Archirel, J. Phys. B **33**, 2409 (2000).

[10] H.J. Beyer, J.B. West, K.J. Ross, and A. De Fanis, J. Phys. B **33**, L767 (2000).

[11] R. Wehlitz and S.B. Whitfield, J. Phys. B **34**, L719 (2001).

[12] A.S. Kheifets and I. Bray, Phys. Rev. A **65**, 012710 (2001).

[13] J. Colgan and M.S. Pindzola, Phys. Rev. A **65**, 022709 (2002).

[14] L. Malegat, P. Selles, and A.K. Kazansky, Phys. Rev. Lett. **85**, 4450 (2000).

[15] S. Fraga, J. Karwowski, and K.M.S. Saxena, *Handbook of Atomic Data* (Elsevier, Amsterdam, 1976).

[16] G.B. Bachelet, D.R. Hamann, and M. Schlüter, Phys. Rev. B **26**, 4199 (1982).

[17] P.J. Hay and W.R. Wadt, J. Chem. Phys. **82**, 270 (1985).

[18] W.R. Wadt and P.J. Hay, J. Chem. Phys. **82**, 284 (1985).

[19] H. Bachau, P. Galan, and F. Martin, Phys. Rev. A **41**, 3534 (1990).

[20] F. Citrini and L. Malegat, J. Phys. B **35**, 1657 (2002).

[21] C.E. Moore, *Atomic Energy Levels* (National Bureau of Standards, Washington, D.C., 1949).

[22] C. Froese Fischer and K.M.S. Saxena, Phys. Rev. A **9**, 1498 (1974).

[23] C. Cohen-Tannoudji, J. Dupont-Roc, and G. Grynberg, *Photons et Atomes: Introduction à l'Electrodynamique Quantique* (InterEditions/Editions du CNRS, Paris, 1987).

[24] J.J. Yeh and I. Lindau, At. Data Nucl. Data Tables **32**, 1 (1985).

[25] K. Berrington, L. Quigley, and H.L. Zhang, J. Phys. B **30**, 5409 (1997).

[26] L.V. Chernysheva, N.A. Cherepkov, and V. Radojevic, Comments Plasma Phys. Controlled Fusion **11**, 57 (1976).

[27] J.A.R. Samson, Z.X. He, L. Yin, and G.N. Haddad, J. Phys. B **27**, 887 (1994).

[28] J.M. Bizau and F.J. Wuillemier, J. Electron Spectrosc. Relat. Phenom. **71**, 205 (1995).

[29] J.A.R. Samson, W.C. Stolte, Z.X. He, J.N. Cutler, Y. Lu, and R.J. Bartlett, Phys. Rev. A **57**, 1906 (1998).

[30] A. Huetz, P. Selles, D. Waymel, and J. Mazeau, J. Phys. B **24**, 1917 (1991).

[31] S. Cvejanovic and T.J. Reddish, J. Phys. B **33**, 4691 (2000).

[32] L. Malegat, P. Selles, P. Lablanquie, J. Mazeau, and A. Huetz, J. Phys. B **30**, 263 (1997).